Received: 8 July 2016 | Accepted: 30 September 2016

DOI: 10.1111/jace.14634

ORIGINAL ARTICLE

Journal of the American Ceramic Society

# Fracture mechanics of sharp scratch strength of polycrystalline alumina

**Robert F. Cook**

Materials Measurement Science Division, National Institute of Standards and Technology, Gaithersburg, Maryland

**Correspondence**
Robert F. Cook, Materials Measurement Science Division, National Institute of Standards and Technology, Gaithersburg, MD
Email: robert.cook@nist.gov

**Abstract**

The strength of a polycrystalline alumina containing controlled scratches introduced by translated sharp contacts is investigated and described by a multiscale fracture mechanics model. Inert strength measurements of samples containing quasi-static and translated Vickers indentation contacts showed that scratches degraded the strength at normal contact loads an order of magnitude less than those for quasi-static indentation. The fracture mechanics model developed to describe strength degradation by scratches over the full range of contact loads included toughening effects by crack-wake bridging at the microscale and lateral crack-based residual stress relaxation effects at the mesoscale. A critical element of the model is the nonlinear scaling of the residual stress field of a scratch with the normal contact load acting during scratch formation. The similarities and differences in the scratch model in comparison with prior indentation-strength fracture mechanics models are highlighted by parallel development of both. Central to the scratch model is the use of easily controlled normal contact load as the scratch-strength measurement variable. Scratch length and orientation are shown to have significant effects on strength. The distributions of scratch widths controlling the intrinsic strengths of as-received samples are determined and agreement with the observed scratch dimensions is demonstrated.

**KEYWORDS**

alumina, fracture, fracture mechanics/toughness, indentation, mechanical properties

## 1 | INTRODUCTION

A recent work[1] demonstrated a multiscale fracture mechanics approach to describe ceramic strengths. In particular, for strengths controlled by sharp contact flaws, an analysis was developed that tied together meso- and microscale effects into a single fracture mechanics framework. At the mesoscale, the framework included the decrease in contact-induced residual stress fields by stress-field relieving lateral cracking and chipping with increasing contact size. At the microscale, the framework included the increase of material fracture resistance with increasing crack length by the formation of microstructurally based crack-closing tractions. Through the use of an effective contact load, the inert strengths of a wide variety of ceramics were described over the full micro-plus-meso flaw-size range. The multiscale framework was shown to be extremely effective in describing the range of strength behaviors of polycrystalline alumina ($Al_2O_3$), a ceramic material that exhibits pervasive, but material-specific, lateral cracking and microstructural traction effects.

The flaws used to demonstrate the fracture mechanics framework were Vickers indentation contacts, shown in the schematic diagrams of Figure 1A,B. The flaws consist of a square-outline residual contact impression imbedded in a localized, almost hemispherical, plastic deformation zone. The strain mismatch between the plastic deformation zone and surrounding elastically deformed matrix leads to a

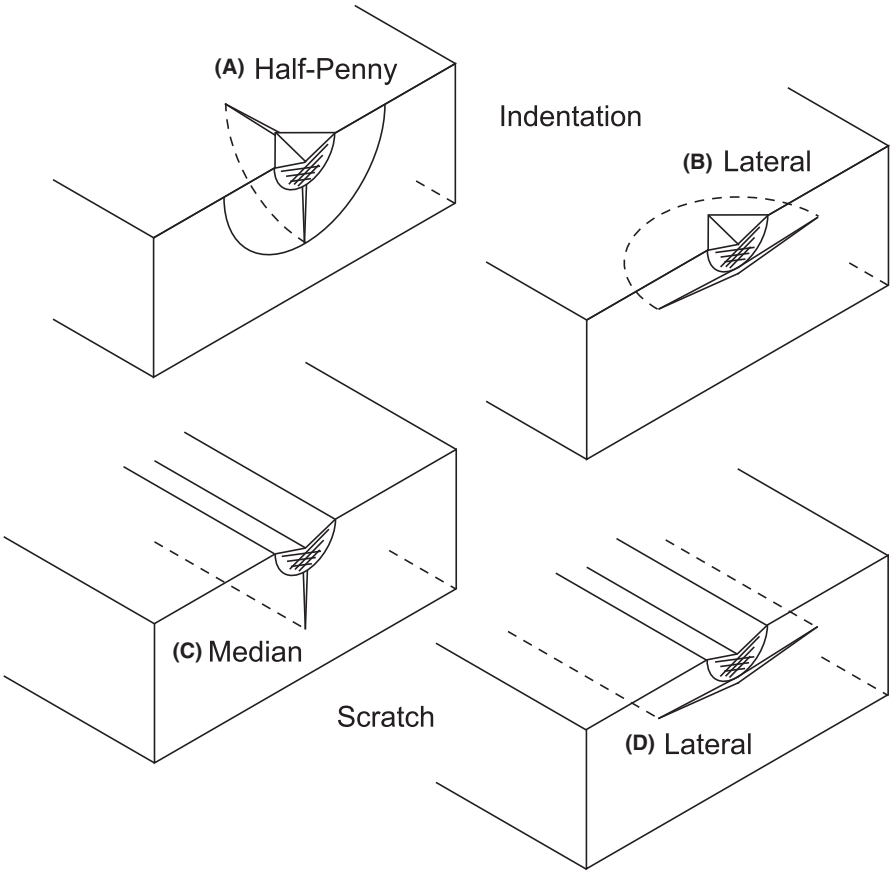


**FIGURE 1** Schematic diagrams of cracking systems at contact flaws: (A) Semicircular half-penny cracks and (B) circular lateral crack at a Vickers indentation; (C) straight median crack and (D) straight lateral crack at a sharp scratch. The straight cracks are formed by the extension of the circular cracks (dashed lines) as a sharp probe is translated over the surface

residual stress field in the matrix that drives two crack systems. The first crack system consists of two crossed, almost semicircular, half-penny cracks propagating perpendicular to the surface,[2] Figure 1A. The second crack system consists of an almost circular lateral crack propagating predominantly parallel to the surface,[3] Figure 1B. There is a threshold indentation load, typically a few newtons for most ceramic materials, for the initiation of half-penny cracks at Vickers indentation contacts. There is a larger threshold load, typically a few tens of newtons, for the initiation of lateral cracks.[4] The half-penny cracks control the strength of a ceramic component containing a Vickers indentation flaw,[5,6] but the lateral cracks diminish the indentation residual stress field acting on the half-penny cracks. As a consequence, strength decreases are limited as indentation load is increased.[7] For many polycrystalline materials, localized tractions behind the crack tip,[8] shown in the schematic diagram of Figure 2A, arising from unbroken ligamentary bridges or frictional interlocks of grains,[9] act to oppose the propagation of the half-penny cracks during a strength test. There is a traction-free crack-propagation distance,[9,10] typically a few tens of micrometers, before the formation of such traction sites, which then increase in number and restraining force as the crack propagates, before eventually saturating at a steady-state restraining influence. As a consequence, strength increases are limited as indentation load (and hence crack size) is decreased.[9,11]

The goal of the present work is to extend the integrated micro- to mesoscale strength framework from point contact flaws typified by sharp indentations to line contact flaws typified by sharp scratches, as well as to investigate the phenomenology of strength control by sharp scratches. Schematic diagrams of such linear flaws are shown in Figure 1C,D. Linear flaws may be formed by a long, straight, sharp wedge,[12-14] a circular, sharp-edged disk rolled over a surface,[15-20] or, as will be considered here, a sharp indenter translated over a surface to form a scratch.[21-32] The loading of the wedge, disk, or indenter is similar to that of the point contact flaw, primarily normal to the surface. Plan and cross-section images of the resulting linear flaws in glass,[12,20,21,24-26] single crystals,[24-26,28] polycrystals,[13,14,23-27,29-31] and rocks[12] all have similar features, Figure 1C,D, all in common with the point flaw of Figure 1A,B: The

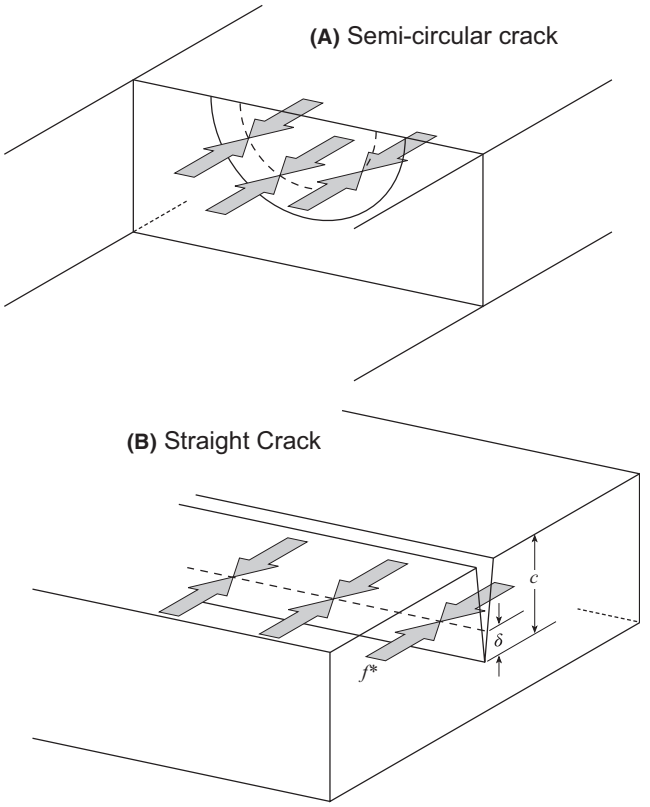


**FIGURE 2** Schematic diagrams of microstructural restraining tractions on crack surfaces: (A) Semicircular distribution on a half-penny crack and (B) straight distribution on a median crack. The tractions are modeled as line forces of magnitude $f^*$ imposed a fixed distance δ behind the crack tip

linear flaw has a rectangular-outline residual contact impression imbedded in an almost semicylindrical plastic deformation zone. The strain mismatch between the zone and the surrounding matrix leads to a residual stress field adjacent to the flaws, as verified by birefringence in cross-polarized light microscopy,[17,19,20] fluorescence shifts in luminescence microscopy,[31,32] and more recently by electron backscatter diffraction and confocal Raman microscopy.[33-35] The residual field drives two crack systems on contact unloading. The first crack system is the single straight median crack or median vent that forms beneath the plastic deformation zone and propagates perpendicular to the surface, Figure 1C. This is the crack system that controls the strength of the component and is the intended outcome of the use of a glass-cutting roller.[18,20] The second linear crack system consists of two straight lateral cracks propagating almost parallel to the surface, Figure 1D. This crack system is often the most visible manifestation of a "scratch" on a brittle material surface,[24] and the system that controls "edge quality" on scored and broken glass components. As with point flaws, lateral cracks influence the strengths of components containing linear flaws by diminishing the residual field acting on the median crack. The importance of (avoiding) lateral cracks in ease of breaking scored glass and obtaining a clean broken edge is highlighted in commercial advice on the subject.[36-38] For linear flaws in polycrystalline materials, the microstructural traction zone acts in a straight line behind the median crack tip, Figure 2B, as opposed to the semicircle for half-penny cracks.

Here, we build on the work, primarily that of Kirchner et al.,[27,39,41-43] in consideration of the strength-degrading nature of scratches, that is, how the strength of a component decreases as an incorporated scratch becomes larger. Following Marshall and Lawn,[5,6] Kirchner et al.[26,39,41-43] combined a stress-intensity factor (SIF) for the residual stress field acting on a straight median crack at a scratch (originally due to Swain and Lawn[12]) with the SIF associated with an applied stress to generate a fracture mechanics analysis for scratch strength.[39,42] This analysis was the beginnings of the current framework, which extends the early analysis with three now-recognized required extensions:[1] (i) mesoscale interactions between the median crack and lateral cracks, Figures 1C,D; (ii) microscale interactions between the median crack and microstructural tractions, Figure 2B; and, (iii) the nonlinear scaling of the experimentally controlled normal contact force and the magnitude of the residual field SIF. The following section describes the materials and methods used to demonstrate the linear flaw strength framework, along with background intrinsic strength and indentation dimension measurements. The material is a polycrystalline $Al_2O_3$ and the primary flaws are scratches formed by a translated loaded Vickers indenter. This is followed by development of the micro-plus-meso scratch strength framework, showing the direct correspondence with the indentation strength framework. Strength degradation results are then presented and the effects of scratch length, orientation, and aging are considered, along with the methodology to estimate strength-controlling scratch dimensions from intrinsic strengths. The Discussion considers the generalizability of the approach.

## 2 | EXPERIMENTAL METHODS AND BACKGROUND OBSERVATIONS

### 2.1 | Materials

The test material was a commercial polycrystalline $Al_2O_3$ (Coors AD995, Golden, CO) consisting of 99.5% by weight $Al_2O_3$ with a grainsize of approximately 5 μm and an as-sintered surface finish of approximately 0.9 μm (center-line average).[44] The material was obtained as cards, 125 mm × 90 mm × 0.65 mm, punched from a larger green sheet prior to sintering. The top of the cards was designated the "A" side and the bottom of the cards, which contained some defects from the punching and handling

operations, was designated the "B" side. Two sample geometries were used: (i) 32 mm × 32 mm for biaxial flexure testing and (ii) 32 mm × 8 mm bars for uniaxial bend testing. Two sets of squares were formed: A-side squares cut from the cards using a high-speed diamond saw and automated robotic handling of the material with the A-side facing the saw blade; and, B-side squares cut from the cards using a high-speed diamond saw but manual handling of the material with the B-side facing away from the saw-blade and contacting the support platen. The B-side squares were anticipated to contain greater surface defects than the A-side squares. The bars were cut from squares in both orientations using manual handling and contained sawing damage on the sawn edges. Some squares were polished to the 0.25 μm diamond level for microstructural and contact damage investigation.

## 2.2 | Strength measurement

The test squares were loaded to failure using a flat-on-three-ball biaxial flexure rig. Alignment pins were located in the base of the rig such that the center of the square specimens and the loading were co-linear. The radius of the upper inner flat, $l_i$, was 2.5 mm and that of the lower outer support circle, $l_o$, in which the three balls sat, 15 mm. Failure stress, σ, was calculated from failure load, $F$, using

$$\sigma = kF/d^2 \tag{1}$$

where $d$ is the specimen thickness. $k$ is a geometry term given by

$$k = (3/2\pi)\{(1+\nu)[\ln(l_o/l'_i) + 1/2] + (1-\nu)\pi l_o^2/2s^2\},$$

where $\nu$ is the Poisson's ratio of the material (here 0.22[44]), $l'_i$ is the (thin-plate) effective inner radius,

$$l_i' = (1.6l_i^2 + d^2)^{1/2} - 0.675d,$$

and $s$ is the edge length of the squares. Using the dimensions of the rig and specimens given, the biaxial geometry constant was calculated as $k$=1.39.

The test bars were loaded to failure in a four-point uniaxial bending rig designed to minimize any torque on the specimens. The upper span was 8.0 mm, the lower span 30 mm, and failure stress calculated from failure load using Equation (1) and a uniaxial geometry term of

$$k = (3/2)(2l_o - 2l_i)/b,$$

where here $2l_o$ is the lower span, $2l_i$ is the upper span, and $b$ is the width of the bar. Using the dimensions of the rig and specimens given, the uniaxial geometry constant was calculated as $k$=4.13.

Strength tests were carried out under inert conditions, using a piezoelectric load-cell to monitor the failure loads. The failure times of approximately 30 ms prevented water and other reactive species in the air from affecting crack propagation during the tests. Figure 3 shows cumulative failure probability as a function of biaxial failure stress for the A- and B-side square samples prepared by automated and manual sawing, respectively. The samples were tested as prepared and the failure stresses thus represent the intrinsic strengths of the samples. Failure for all included biaxial flexure samples originated in the center of the tensile face in the uniformly stressed region beneath the upper flat. At least 50 strength tests were performed for each preparation method. The resulting intrinsic strength values were (A-side) (713 ± 69) MPa and (B-side) (669 ± 90) MPa. (Unless otherwise noted, all quantities and uncertainties are given in this work as mean ± standard deviation of experimental values.) The strength distributions overlap considerably and although the A sides exhibited greater strength than the B sides, there was not a significant difference in the mean intrinsic strength. The axes in Figure 3 are drawn such that straight-line behavior indicates a normal distribution of strengths. Both distributions in Figure 3 exhibit convex behavior, indicative of strength distributions

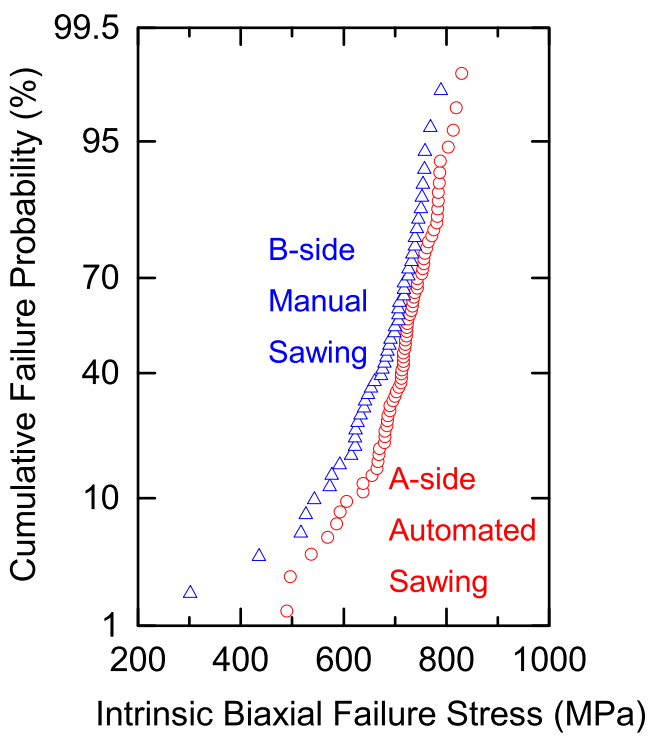


**FIGURE 3** Cumulative failure probability as a function of biaxial failure stress for polycrystalline $Al_2O_3$ containing strength-controlling flaws intrinsic to the material and two different sample preparation sawing methods [Color figure can be viewed at wileyonlinelibrary.com]

that contain more weaker, low strength, samples than a normal distribution. This is particularly evident for the manually sawn B-side samples. An implication is that defects generated on the B sides of samples by contacts during manual loading for sawing are significantly more severe than the incoming defects on the A sides, but that there are relatively few of these B-side defects. This point will be taken up in the Results in the context of flaw-size estimation. A similar strength distribution was obtained from uniaxial strength testing of more than 100 as-prepared bar samples. The uniaxial strengths were (645 ± 85) MPa, less than the biaxial strengths although the difference is barely significant. There was no significant difference in uniaxial strengths between A- and B-side bar samples. Failure for all included uniaxial bend samples originated on the tensile face in the uniformly stressed region beneath the upper span; for the as-prepared bars, failure originated at or near the edge of the bar, suggesting significant effect of sawing damage.

## 2.3 | Controlled flaws

Before strength testing, a controlled flaw was deliberately introduced into the prospective tensile face of many of the test specimens to reduce the strength below the intrinsic or sawing damage limits. For the biaxial tests, the controlled flaws were centered on the specimen under the loading flat. For the uniaxial tests, the controlled flaws were centered on the specimen between the upper span points. Controlled flaws were introduced into the specimens using two techniques: (i) Indentation using a Vickers diamond pyramid (Indentation) and (ii) Scratching using a Vickers diamond pyramid (Scratch). The scratch flaws were produced by loading the specimen with the Vickers indenter and translating the specimen under the indenter via the specimen stage controls. The translation speed was approximately 0.5 mm/s and translation was parallel to a pyramidal edge.

The advantage of such indentation and scratch flaws is that the scale of the flaw may be controlled by the applied normal contact load, $P$, here over the range (0.25-100) N for the indentations and (0.013-5) N for the scratches. Figure 4 shows the variation of Vickers indentation contact impression semidiagonal, $a$, as a function of $P$, measured on polished squares; a schematic plan diagram of the indentation contact dimensions is shown in Figure 5A. The symbols represent the means and standard deviations of at least four measurements at each load. The solid line is a slope 1/2 best-fit to the data, consistent with constant hardness:

$$H = P/2a^2 \tag{2}$$

The value of $H$=(17.4 ± 0.5) GPa was found, intermediate to polycrystalline $Al_2O_3$ materials with greater and lesser $Al_2O_3$ fractions.[1,45]

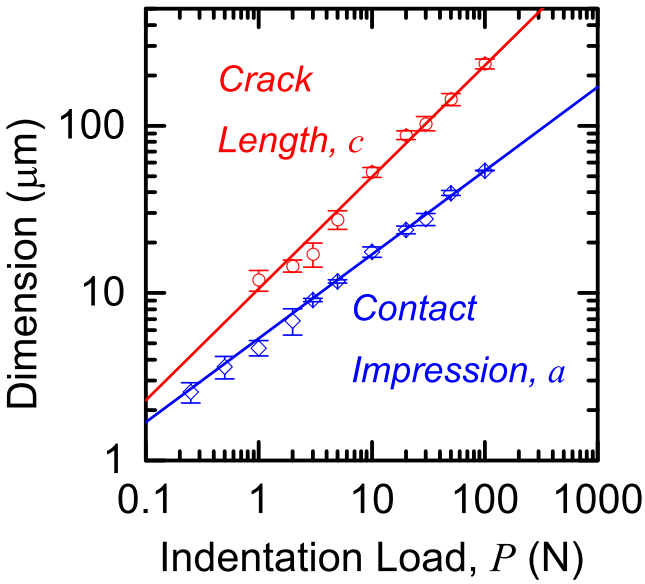


**FIGURE 4** Indentation crack length and contact impression dimensions as a function of indentation load for Vickers indentation of a polycrystalline $Al_2O_3$ [Color figure can be viewed at wileyonlinelibrary.com]

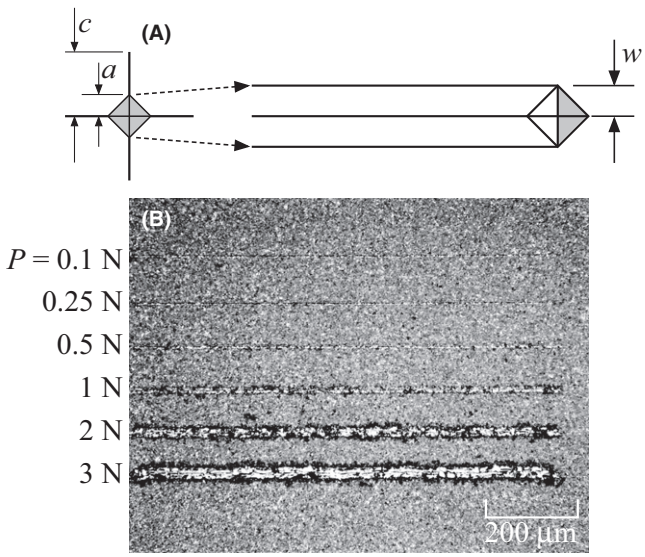


**FIGURE 5** (A) Schematic plan view diagram of a static Vickers indentation with crack length and contact impression dimensions indicated and schematic plan view of a translating Vickers indenter forming a scratch with track width indicated. The areas of the indenter supported by the material during loading are shaded. (B) Optical micrograph of scratch tracks formed by a translated Vickers indenter on the surface of a polycrystalline $Al_2O_3$ using normal contact loads indicated

Figure 4 also shows the variation in the half-penny crack surface-trace length, $c$, (measured from the impression center). The symbols represent the means and standard deviations of eight measurements at each load above the threshold load of 1 N. Over the domain of loads for which

cracks were observed, the crack-length data are well-described by a slope 2/3 dependence, consistent with a constant toughness/crack geometry ratio:

$$T_{air}/\chi_0 = P/c^{3/2} \tag{3}$$

$T_{air}$ is the toughness in (moisture-containing) air and $\chi_0$ is a dimensionless constant quantifying the effects of the indentation stress-field and crack geometry in the absence of any applied stress or consequent extension of the half-penny cracks. The value of $P/c^{3/2}$=(27.2 ± 1.9) MPa $m^{1/2}$ was found, slightly less than values observed for other polycrystalline $Al_2O_3$ materials in an inert (moisture-free) environment.[45]

Figure 5B shows Vickers indenter scratch tracks on the surface of the $Al_2O_3$ produced as described above using different applied normal loads. The average width of the tracks increased with load, as did the width uniformity. The tracks appear to consist primarily of plastic deformation, with some localized chipping on the track edges at the larger loads, similar to that observed for scratches at similar loads in polycrystalline $Al_2O_3$[23,25,26,29,30] and other materials;[24,27,28,31,32] there was no obvious lateral cracking and material removal by chipping as observed in some single crystals.[24,29,30] As noted above, the advantage of such controlled-flaw scratches is that the scale can be controlled by the applied normal load, and that will be the major focus here. In addition, the effects on strength of scratch length, orientation and position, and environmental exposure can also easily be controlled.

A schematic plan diagram in Figure 5A shows the track dimensions and the supported contact area during scratch formation by a Vickers indenter, assuming no elastic recovery of the formed track such that the material supports the indenter only on the front two pyramidal faces. The transition from static indentation (left) to steady-state scratching (right) (similar to that for static to rolling contact for a conical roller[20]) is indicated by the dashed lines and for illustration is exaggerated in length. The major visible features of the transition are an increase in the width of the contact impression track and a suppression of the formation of half-penny cracks perpendicular to the scratching direction. Assuming invariant hardness, the half-width of the steady-state track, $w$, is given by

$$H = P/w^2 \tag{4}$$

and thus, combining Equations (2) and (4), $w = \sqrt{2}a$. Comparison of the track width at 3 N, $2w \approx 30$ μm (Figure 5B) with the contact diagonal, $2a \approx 20$ μm (Figure 4), at the same load is consistent with this relation. The half-penny cracks parallel to the scratching direction are the precursor to the median vent (Figure 1) and are not visible on the surface, but in the case of the 3 N scratch are likely about 20 μm deep (Figure 4); the lateral cracks are likely to be somewhat less in extent.[21,25-30,42,43]

## 3 | SCRATCH STRENGTH DEGRADATION ANALYSIS

Here, a fracture mechanics model is developed to describe the strength degradation of components by sharp scratches. The development is deliberately made parallel with the much more commonly applied fracture mechanics models of strength degradation by indentation[1,5,6] so as to highlight the similarities and differences.

Under the influence of a subsequently applied uniform stress (here from biaxial flexure or uniaxial bending), a contact flaw (here indentation, scratch, or wedge) with its attendant residual stress field, has a two-component SIF $K$:

$$K = K_r + K_a \qquad \text{(indentation)}, \tag{5a}$$

$$K = K_s + K_a \qquad \text{(scratch)}, \tag{5b}$$

$$K = K_w + K_a \qquad \text{(wedge)}, \tag{5c}$$

where the applied SIF, $K_a$, is common to all three contact flaws and Equation (5) is written to emphasize that the scratch geometry is intermediate to indentation and wedge. For a pyramidal contact giving rise to a sharp indentation (Figure 1A), the residual SIF, $K_r$, acting on the half-penny crack (Equation 5a) is stabilizing ($dK_r/dc < 0$) and given by

$$K_r = \chi P/c^{3/2} \qquad \text{(indentation)}, \tag{6}$$

where $P$ is the indentation load, $c$ is the radius of the half-penny crack, and $\chi$ is a general value, for non-zero applied stress, of the dimensionless factor quantifying the effects of the indentation stress-field and crack geometry. For a wedge contact giving rise to a line flaw (Figure 1C), the residual SIF, $K_w$, acting on the median crack (Equation 5c) is also stabilizing ($dK_w/dc < 0$) and given by

$$K_w = \chi_w P_w/c^{1/2} \qquad \text{(wedge)}, \tag{7}$$

where $P_w$ is the contact load per length of the wedge, $c$ is the depth of the median crack, and $\chi_w$ is the dimensionless factor quantifying the effects of the wedge stress-field and crack geometry. Before application of the applied stress, the cracks have stable, initial equilibrium lengths, $c_i$, given by setting $K_r$=$T_{air}$ or $K_w$=$T_{air}$ and inverting Equations (6) and (7) to arrive at

$$c_i = (\chi P/T_{air})^{2/3} \qquad \text{(indentation)}, \tag{8}$$

$$c_i = (\chi_w P_w/T_{air})^2 \qquad \text{(wedge)}. \tag{9}$$

Equation (8) is identical to Equation (3) above and is represented in Figure 4 in describing the half-penny crack

lengths of the $Al_2O_3$. Equation (9) is that derived and used in an earlier work[12] to describe the lengths of median cracks formed by wedge indentation of glass.

For formation of a linear flaw and crack system shown in Figure 1C,D by extended wedge indentation, the relationship between the load per length $P_w$ and the normal load $P$ is simple and linear: $P_w=P/L$, where $L$ is the length of the wedge. Plane-strain conditions perpendicular to the linear flaw are maintained during and after the wedge indentation process. For formation of a linear flaw and crack by localized translated or rolled contacts, the relationships between $P_w$ and the normal contact load $P$ are nonlinear. The simplest relationship is that for a translated probe in which the included probe angle is invariant in planes parallel and perpendicular to the translation direction (i.e., the probe is geometrically similar in both planes). Examples include a pyramid (eg, a Vickers indenter) translated perpendicular to the pyramid axis or a short prism (eg, as drawn in Ref. [19]) translated parallel to the prism axis. During contact, if the translation is slow or quasi-static, the deformation field adjacent to the probe is similar to that of an indentation. After contact, once the probe has formed a linear scratch, plane strain conditions perpendicular to the scratch pertain, similar to that for the extended wedge indentation. The similarity of the final equilibrium deformation states enables the relation between $P_w$ and $P$ to be obtained by enforcing equivalency of the widths of the contact impressions. In the translated probe cases, the supported contact stress, the hardness $H$, is given by Equation (4), $P/w^2=H$, as shown in the schematic diagram of Figure 5A and Ref. [19]. In the case of the extended wedge indentation, the supported contact stress is given by $P_w/2w=H$. Eliminating $w$ from these two equations gives $P_w \sim P^{1/2}$ and thus the residual SIF for the scratch-induced median crack, $K_s$, (Equation 5b) expressed in terms of the normal load is given by

$$K_s = \chi_s P^{1/2}/c^{1/2} \qquad \text{(scratch)}, \tag{10}$$

This load dependence for the scratch residual SIF is central to the fracture mechanics analysis for strength developed here. (The development of this SIF by Symonds et al.[19] using the equivalency analysis for geometrically similar translated contacts was not used by them as all the tests were conducted at one load, and, in fact, would not have been applicable as the flaws therein were made by a conical roller which does not maintain geometrical similarity with contact depth; a roller analysis[20] is needed). $\chi_s$ quantifies the general value of the effects of the scratch residual stress field on the linear scratch crack and has dimensions of $[\text{stress}]^{1/2}$. Setting equilibrium and inverting Equation (10) as above gives the length of the median crack formed at a scratch by a geometrically similar probe as

$$c_i = (\chi_s P^{1/2}/T_{air})^2 \qquad \text{(scratch)}. \tag{11}$$

The linear variation in median crack length with normal load at scratches suggested by Equation (11), $c_i \sim P$, is consistent with the limited clear experimental observations[43,46] (in other experimental works the plotting scheme used, following Equations (8) and (9), and using $P$ for $P_w$ precludes clear assessment[26]).

The applied SIF $K_a$ is destabilizing ($dK_a/dc > 0$) and is given by

$$K_a = \psi_{(s)}\sigma_a c^{1/2}, \tag{12}$$

where $\sigma_a$ is the applied stress, $c$ is the crack length, and $\psi_{(s)}$ is a dimensionless geometry factor, characterizing the effects of the applied stress on the crack and takes different values for the indentation and scratch (subcript "s") flaws. The applied stress causes failure of a component from a contact flaw at a stable-to-unstable transition found by simultaneously imposing equilibrium, $K=T_0$ (Equations 13 below), where the toughness $T_0$ is here taken to be an invariant inert value in the absence of any reactive species, and instability, $dK/dc = dT_0/dc = 0$ (Equations 14 below). Combining Equations (5a, 5b, 6, 10, and 12) gives for these two conditions for each flaw:

$$\chi P/c^{3/2} + \psi\sigma_a c^{1/2} = T_0, \qquad \text{(indentation)} \tag{13a}$$

$$\chi_s P^{1/2}/c^{1/2} + \psi_s\sigma_a c^{1/2} = T_0, \qquad \text{(scratch)} \tag{13b}$$

and

$$3\chi P/c^{3/2} - \psi\sigma_a c^{1/2} = 0, \qquad \text{(indentation)} \tag{14a}$$

$$\chi_s P^{1/2}/c^{1/2} - \psi_s\sigma_a c^{1/2} = 0, \qquad \text{(scratch)} \tag{14b}$$

where the notation (a, indentation) and (b, scratch) will be used throughout. Combining Equations (13a) and (14a) and Equations (13b) and (14b) gives the crack lengths at instability for each flaw type:

$$c_{max} = (4\chi P/T_0)^{2/3} \approx 4^{2/3}c_i, \qquad \text{(indentation)} \tag{15a}$$

$$c_{max} = (2\chi_s P^{1/2}/T_0)^2 \approx 4c_i, \qquad \text{(scratch)} \tag{15b}$$

using Equations (8) and (11), and the stresses at instability —the component strengths—for each flaw type:

$$\sigma_{max} = 3T_0/4\psi c_{max}^{1/2} = 3T_0^{4/3}/4^{4/3}\psi\chi^{1/3}P^{1/3}, \qquad \text{(indentation)} \tag{16a}$$

$$\sigma_{max} = T_0/2\psi_s c_{max}^{1/2} = T_0^2/4\psi_s\chi_s P^{1/2}. \qquad \text{(scratch)} \tag{16b}$$

The subscript "max" in Equations (15) and (16) indicates that these are the ($\sigma$, $c$) configurations at the maximum sustainable equilibrium stress for flaws generated at

contact load $P$. The expression for scratch strength, Equation (16b), involving $c_{max}$ was derived by Kirchner,[39,42] but the use of Equation (7) rather than Equation (10) led to an incorrect experimental indentation load dependence.

The expressions in Equation (16) are for "ideal" contact flaw strength variations with contact load,[1] and are the asymptotic limits for strength at intermediate loads between micro- and meso-dominated effects. The effect of increasing the load is to increase the tendency to lateral cracking at the contact with a consequent reduction in the residual stress field. This reduction is characterized by modifications to the $\chi$ terms:

$$\chi = \chi_0/(1 + P/P_L), \qquad \text{(indentation)} \qquad (17a)$$

$$\chi_s = \chi_{0s}/[1 + (P/P_L)^{1/2}], \qquad \text{(scratch)} \qquad (17b)$$

scaling the decrease in $\chi_{(s)}$ linearly with the increase in the residual stress field driving element $P$ or $P^{1/2}$. The decrease arises from decreased constraint on the contact-induced plastic deformation zone as lateral cracks decouple the zone from the surrounding matrix (Figure 1); Equations (17) reflect a linear scaling with driving element of the (lateral crack)/(plastic deformation zone) volume ratio.[7] The $P_L$ values characterize the contact load above which lateral cracking and residual stress field relief become significant. Effective contact loads are $P_{(s)}^{\sim}$ defined such that the residual SIF is linear in the effective load:

$$\tilde{P} = P(1 + P/P_L), \quad \text{such that} \chi P = \chi_0 \tilde{P}, \qquad \text{(indentation)} \qquad (18a)$$

$$\tilde{P}_s^{1/2} = P^{1/2}[1 + (P/P_L)^{1/2}], \quad \text{such that} \quad \chi_s P^{1/2} = \chi_0 \tilde{P}_s^{1/2}. \qquad \text{(scratch)} \qquad (18b)$$

Simple modification of Equations (16a) and (16b) by replacing $\chi_{(s)}$ by $\chi_{0(s)}$ and $P$ by $P_{(s)}^{\sim}$ yields the contact-flaw strength behavior including the effects of lateral cracking at large loads:

$$\sigma_{max} = 3T_0^{4/3}/4^{4/3}\psi\chi_0^{1/3}\tilde{P}^{1/3} = \sigma_{max}^L(1 + P_L/P)^{1/3}, \qquad \text{(indentation)} \qquad (19a)$$

$$\sigma_{max} = T_0^2/4\psi_s\chi_{0s}\tilde{P}^{1/2} = \sigma_{max}^L\left[1 + (P_L/P)^{1/2}\right], \qquad \text{(scratch)} \qquad (19b)$$

where the characteristic lateral-crack corrected strengths are given by

$$\sigma_{max}^L = 3T_0^{4/3}/4^{4/3}\psi\chi_0^{1/3}P_L^{1/3}, \qquad \text{(indentation)} \qquad (20a)$$

$$\sigma_{max}^L = T_0^2/4\psi_s\chi_{0s}P_L^{1/2}. \qquad \text{(scratch)} \qquad (20b)$$

The general relations of Equations (19a) and (19b) exhibit concave-up responses, tending to the inverse-load dependences of Equations (16a) and (16b) at small loads and the load-invariant strengths of Equations (20a) and (20b) at large loads.

A further, final effect is that of increasing toughness with crack length, which in $Al_2O_3$ materials derives from grain interlocking and bridging behind the crack tip. The toughness increase is described by a crack-length dependent addition to the inert base toughness $T_0$ to give the full toughness response:

$$T = T_0 + \mu f^* \delta^{-1/2}\left[1 - (\delta/c)^{3/2}\right], \qquad \text{(indentation)} \qquad (21a)$$

$$T = T_0 + \mu f^* \delta^{-1/2}\left[1 - (\delta/c)^{1/2}\right], \qquad \text{(scratch)} \qquad (21b)$$

where the different crack length dependences arise from the different number of restraining bridging elements generated by propagating circular or straight crack fronts.[47,48] The parameter $f^*$ characterizes the average restraining force per unit length that the bridging elements exert on the crack periphery and $\delta$ characterizes the average distance behind the crack front at which the restraint acts, Figure 2. $\mu$ is a dimensionless geometrical factor. There is an asymptotically upper limiting value of the toughness at large crack lengths ($c \gg \delta$) given by

$$T_\infty = T_0 + \mu f^* \delta^{-1/2}, \qquad (22)$$

at which the bridging elements take-up a steady-state configuration. From an internal, crack-tip, frame of reference, the bridging elements appear as a negative SIF, $K_\mu(c) < 0$, added to right side of Equations (5) to make a three-component SIF, and the "toughness" is invariant at $T_0$. Equations (21) and (22) view the system from the external frame of reference that is important for predicting component responses to contacts and applied stresses and treat the bridging elements as crack-length-dependent "toughening", $T_\mu(c) = -K_\mu(c) > 0$.[1]

Characteristic microstructure-related contact loads $P_{*(s)}$ may be defined, less than which the crack lengths are small enough that variations in toughness become significant:

$$\chi_0 P_* = \mu f^* \delta, \qquad \text{(indentation)} \qquad (23a)$$

$$\chi_{0s} P_{*s}^{1/2} = \mu f^*. \qquad \text{(scratch)} \qquad (23b)$$

Simple modification of Equations (19a) and (19b) by replacing $T_0$ by $T_\infty$ and $\tilde{P}$ by $(\tilde{P} + P_*)$or $\tilde{P}_s^{1/2}$by $(\tilde{P}_s^{1/2} + P_{*s}^{1/2})$ yields the contact-flaw strength behavior, including the effects of lateral cracking at large loads and toughening at small loads:

$$\sigma_{max} = 3T_\infty^{4/3}/4^{4/3}\psi\chi_0^{1/3}(\tilde{P} + P_*)^{1/3} = \sigma_{max}^*[1 + (P/P_*)/(1 + P/P_L)]^{-1/3}, \qquad \text{(indentation)} \qquad (24a)$$

$$\sigma_{max} = T_{\infty}^2/4\psi_s\chi_{0s}(\tilde{P}_s^{1/2} + P_{*s}^{1/2})$$
$$= \sigma_{max}^*\left[1 + (P/P_{*s})^{1/2}/(1 + (P/P_L)^{1/2})\right]^{-1} \quad \text{(scratch)} \quad (24b)$$

where the characteristic toughening-corrected strengths are given by

$$\sigma_{max}^* = 3T_{\infty}^{4/3}/4^{4/3}\psi\chi_0^{1/3}P_*^{1/3}, \quad \text{(indentation)} \quad (25a)$$
$$\sigma_{max}^* = T_{\infty}^2/4\psi_s\chi_{0s}P_{*s}^{1/2}. \quad \text{(scratch)} \quad (25b)$$

The relations of Equations (24a) and (24b) include an approach to the load-invariant strengths of Equations (25a) and (25b) at small loads, such that the general response is sigmoidal: concave-down at small loads and concave-up at large loads.[1,48] The asymptotic limits of Equations (24a) and (24b) are thus: the microstructural-dominated strengths at small loads (microscale),

$$\sigma_{max} \to \sigma_{max}^* \text{for} P \ll P_{*(s)}, \quad (26)$$

the residual stress-field-dominated strengths at intermediate loads,

$$\sigma_{max} \to \sigma_{max}^*(P/P_*)^{-1/3} \text{for} P_* \ll P \ll P_L, \quad \text{(indentation)} \quad (27a)$$
$$\sigma_{max} \to \sigma_{max}^*(P/P_{*s})^{-1/2} \text{for} P_{*s} \ll P \ll P_L, \quad \text{(scratch)} \quad (27b)$$

and, the chipping-dominated strengths at large loads (mesoscale),

$$\sigma_{max} \to \sigma_{max}^*(P_L/P_*)^{-1/3}$$
$$= \sigma_{max}^L \quad \text{for} P \gg P_L, \quad \text{(indentation)} \quad (28a)$$
$$\sigma_{max} \to \sigma_{max}^*(P_L/P_{*s})^{-1/2} = \sigma_{max}^L \text{for} P \gg P_L. \quad \text{(scratch)} \quad (28b)$$

## 4 | RESULTS

### 4.1 | Strength degradation

Degradation of the intrinsic strength by contact flaws was examined using the A-side squares. Sharp indentations or sharp scratches (5 mm long) were placed in the centers of specimens over a load range of 0.013 to 100 N. The specimens were tested as for the intrinsic strength tests and every specimen was examined by optical microscopy after failure to ascertain failure or otherwise from the contact flaw. Figure 6 shows the strength degradation results for both flaws. The upper shaded band represents the mean and standard deviation intrinsic strength limits of the A-side squares, and individual symbols represent individual contact-flaw failures at the load and strength indicated. At very small loads (and hence very small flaws), some specimens did not break from the introduced contact flaw but broke from a pre-existing intrinsic flaw; these specimens are not included in Figure 6. Figure 6 indicates that sharp scratches were more potent than indentation flaws in degrading strength at the same contact load; extremely small scratch loads, of order 0.01 N (1 gf), were able to degrade the strength of "pristine" A-side squares, whereas loads approximately an order of magnitude greater were required for indentations.

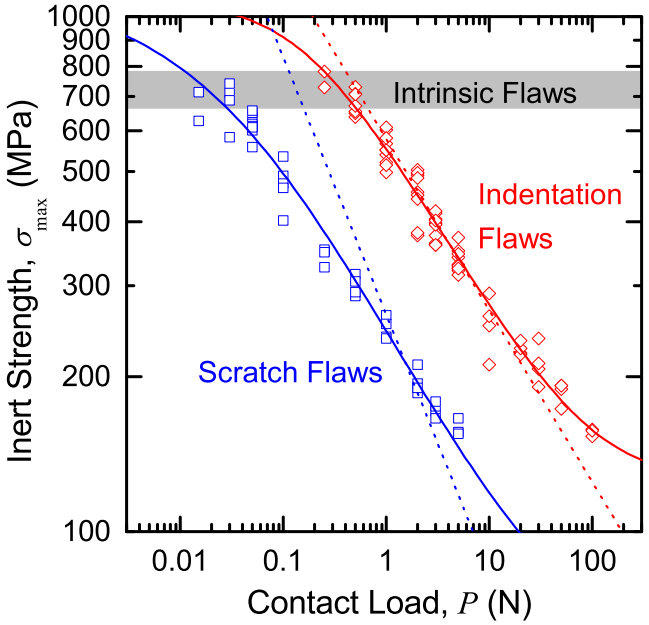


**FIGURE 6** Inert strength as a function of contact load for a polycrystalline $Al_2O_3$ containing indentation and sharp scratch flaws. The solid lines are best fits to the strength data using fracture mechanics models that incorporate microscale toughness effects at small loads and mesoscale stress-relief effects at large loads. The dashed lines represent ideal contact flaw strength behavior not influenced by either of these effects [Color figure can be viewed at wileyonlinelibrary.com]

Best-fits to the indentation and scratch strength data were made using Equations (24a) and (24b) and are shown as the solid lines in Figure 6. The dashed lines in Figure 6 are the ideal contact flaw asymptotes, Equations (27a) and (27b), derived from the fits and characterized by $\sigma_{max}^* P_*^{1/3}$=578 MPa N$^{1/3}$ and $\sigma_{max}^* P_{*s}^{1/2}$=263 MPa N$^{1/2}$ for the indentations and scratches, respectively. The indentation flaws best exemplify the ideal dependence as an intermediate asymptote: at small indentation loads, the measured strengths are less than this asymptote as microscale variations in toughness with crack length become significant and the strengths approach the invariant upper bound of $\sigma_{max}^*$, Equation (26); at large indentation loads, the measured strengths are greater than the ideal asymptote as

mesoscale lateral-crack stress relaxation effects become significant and the strengths approach the invariant lower bound of $\sigma^{L}_{max}$, Equation (28a). In this $Al_2O_3$ material, both these effects are relatively mild over the indentation load range tested and at intermediate loads the measured strengths lie on the ideal asymptote, similar to observations of other relatively small-grained $Al_2O_3$ materials (eg, AD90 and AD999[1,11]). Larger grain sizes and greater indentation load ranges lead to much greater deviations, such that the ideal response does not describe the measured strengths over any load range (eg, the Vistal-based materials[1,11,48]).

The solid line best-fit response for the scratch flaws in Figure 6 bears superficial similarity to that for the indentation flaws shifted to smaller contact loads. This shift is quantified by the reduced characteristic indentation loads for the scratch flaws of $P_{*s}$=(0.054 ± 0.024) N and $P_L$=(28 ± 37) N for the onsets of micro- and mesoscale behavior, respectively, relative to $P_*$=(0.155 ± 0.040) N and $P_L$=(97 ± 46) N for the indentation flaws (uncertainties represent standard deviations of the fit parameters). The indentation measurements filled the load range between $P_*$ and $P_L$, whereas the scratch measurements were in a load range substantially less than the analogous value of $P_L$ and extended across $P_{*s}$. The *quantitative* shift characterizes a *qualitative* difference in the mechanics for the two flaws: The much shorter cracks associated with the scratch flaws experienced increases in toughness (Equation 21b) toward the steady-state level (Equation 22) with increasing flaw and crack size, whereas the longer indentation cracks experienced almost no change in toughness from the steady-state level. Hence, although the best-fit responses in Figure 6 look similar, the scratch response (solid line) exhibits much greater deviation from the ideal asymptote (dashed line) at small contact loads. Both flaw types approached similar invariant microscale strength values, $\sigma^{*}_{max}$=(1076 ± 79) MPa for the indentation flaws and $\sigma^{*}_{max}$=(1131 ± 165) MPa for the scratch flaws, consistent with microstructural control of strength independent of the nature of the flaw. The invariant mesoscale strength values for the two flaw types were different, $\sigma^{L}_{max}$=(126 ± 19) MPa for the indentation flaws and $\sigma^{L}_{max}$=(50 ± 22) MPa for the scratch flaws, consistent with the dependence of lateral cracking and stress relief on flaw type. The following sections examine the variations in the strength-degrading potency of the scratch flaws as a function of scratch length and scratch orientation.

## 4.2 | Scratch length effects

Figure 7 is a plot of the strength of A-side squares containing 0.1 N sharp scratches of various lengths. The relationship between $w$ and $a$, and the measurements in Figure 4 suggest the scratch width $2w$ was about 5 μm. The

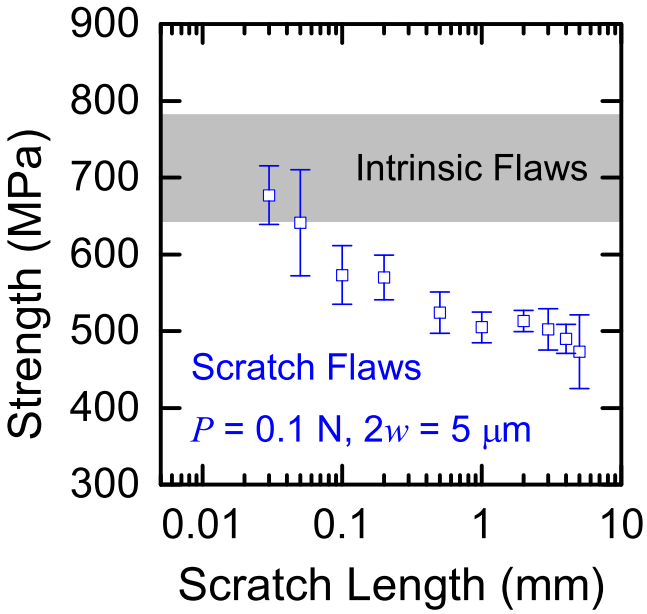


**FIGURE 7** Strength of a polycrystalline $Al_2O_3$ containing sharp scratch flaws of various lengths [Color figure can be viewed at wileyonlinelibrary.com]

symbols represent the means and standard deviations of five strength tests at each length. The shaded band represents the mean and standard deviation limits of the intrinsic strength. The symbol to the extreme right represents the scratch length, 5 mm, that was used in the strength degradation study of Figure 6. Decreasing the scratch length by an order of magnitude to 500 μm did not change the strength significantly, although there was a slight increase. Further decreases in length increased the strength significantly until the intrinsic strength level was reached for scratches 30 μm long. An interpretation of Figure 7 is that sharp scratch flaws in this polycrystalline $Al_2O_3$ varied in their strength-degrading ability along their length. That is, variations in microstructure from point to point along the scratch path led to variations in crack depth, crack orientation, and material toughness from point to point along the crack front and hence to local variations in the maximum sustainable stress. Figure 6 suggests that variations in lateral crack effects and hence variations in residual field along the scratch length were not a factor at this scratch load. The scratch will begin to fail at the point with the smallest sustainable stress and this point is thus the most potent at degrading the component strength. For scratches longer than 500 μm (about 100 times the width and probably about 500 times the median crack depth, Figure 4), the probability of generating a maximally potent point appeared to be guaranteed and the strength approached a length-invariant minimum. For scratches shorter than 500 μm, the most strength-degrading point of the scratch appeared to decrease in potency, until, for scratches shorter

than about 30 μm (about six times the width), the probability of any point along the scratch being more potent at degrading the strength than an intrinsic flaw was zero.

## 4.3 | Scratch orientation effects

The effect of scratch orientation on strength was studied using 1-mm long scratches formed with a normal contact load of 1 N at various angles θ to the tensile axis of uniaxial bend bars. Figure 8 is a plot of the strength as a function of scratch angle to the tensile axis. Symbols with error bars represent the means and standard deviations of five tests at each angle, and individual symbols represent individual strength tests. The lower shaded band in Figure 8 represent the strengths $\sigma_{90}$ of θ=90° scratches lying perpendicular to the tensile axis. The upper shaded band represents the mean and standard deviation limits of the 1 N indentation flaw strengths from Figure 6. As the angle to the tensile axis θ decreased, the strengths increased and (not shown) the probability of failure from the introduced scratch decreased. The strengths increased with decreasing angle to the tensile axis until the indentation strength limit was reached. Along with the increase in strength, there was also a change in failure morphology, as shown in the series of micrographs of Figure 9. In the micrographs, the tensile axis is horizontal and the scratches appear as pale lines. For 90° and 75° scratches, the crack extending to cause failure followed the scratch track closely along its entire length, Figure 9A. For 60°, 45°, and 30° scratches, the extending cracks followed the scratch track for only a limited distance before diverging to propagate perpendicular to the tensile axis, Figure 9(B). Extension along the scratch track decreased with decreasing angle. Once again an interpretation is that the cracks initiated at the most potent point along the scratch length. For 15° and 0° scratches, the cracks initiated at the ends of the scratches and almost immediately propagated perpendicular to the tensile axis, Figure 9C. The implication in this case is that the strength was controlled by the point-flaw-like indentation contacts at the ends of the scratches, Figure 5B.

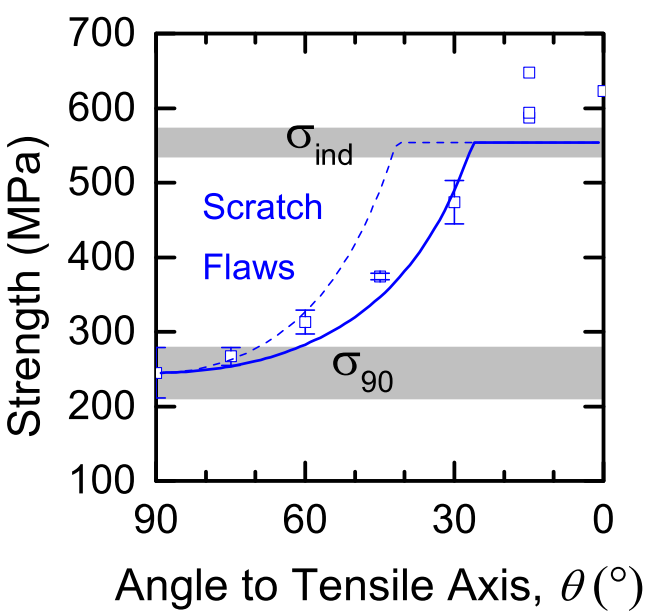


**FIGURE 8** Strength of a polycrystalline $Al_2O_3$ containing sharp scratch flaws at various orientations to the tensile axis of bend bars [Color figure can be viewed at wileyonlinelibrary.com]

The strength increase with decreasing angle can be described empirically by

$$\begin{aligned}\sigma &= \sigma_{90}/\cos(\pi/2-\theta) for \theta \geq \theta_s, \\ &= \sigma_{ind} \quad \text{for} \quad \theta < \theta_s\end{aligned}, \tag{29}$$

where $\theta_s$ is an angle at which the scratch characteristics dominate the indentation characteristics:

$$\theta_s = \pi/2 - \cos^{-1}(\sigma_{90}/\sigma_{ind}), \tag{30}$$

and $\sigma_{ind}$ is the indentation strength. $\theta_s$ was about 28° here. The lower solid line in Figure 8 shows the fit from Equations (29) and (30) for the oriented scratch data and describes the observations well. The upper dashed line in Figure 8 shows a prediction by projection of the applied stress on the flaw, varying as $\cos^2(\pi/2 - \theta)$ in Equation (29), and overpredicts the strength increase with decreasing angle, probably as a consequence of the omission of mixed-mode fracture analysis. The factor of just over two in strength increase from 90° to 0° scratches is consistent with some of the earliest studies.[22] There was no effect on strength of scratch placement. Specimens containing 0.1 N, 1 mm scratches placed 20 μm from the edge of the bend bars exhibited identical strengths to those containing scratches 2 mm from the edge and in the center of the bars (4 mm from edge). The uniaxial bend strengths of scratched bars were identical to those of scratched biaxial flexure disks.

## 4.4 | Aging effects

Exposure to reactive environments can often alter the geometry of contact flaws, principally by reducing the residual stress field through the enhanced growth of lateral cracks.[49] Figure 10 plots the inert strength of biaxially stressed squares containing 3 N indentations or 0.1 N, 5 mm scratch flaws exposed to distilled water. The squares were indented or scratched in air, immersed in distilled water for various periods of time, and removed and dried with an air gun immediately before testing under inert conditions (along with some un-immersed controls). Such a test mimics the introduction of a contact flaw during a grinding operation with consequent exposure to cooling water and varying periods between grinding, drying, and

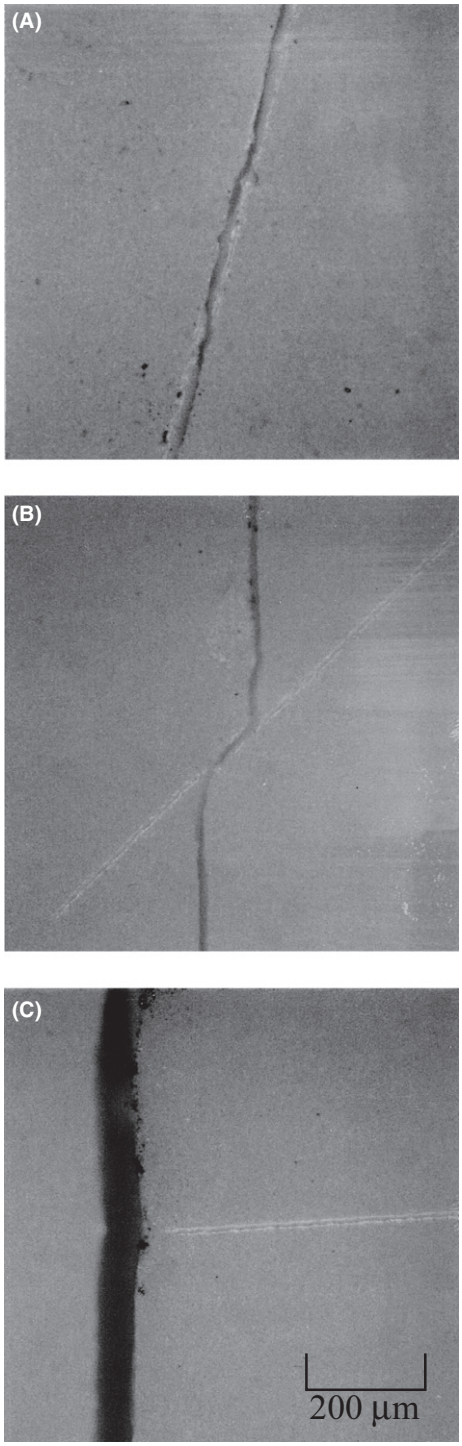


**FIGURE 9** Optical micrographs of the failure locations of a polycrystalline $Al_2O_3$ containing scratch flaws at (A) 75°, (B) 45°, and (C) 0° to the tensile axis of bend bars

subsequent stressing of a component. The symbols in Figure 10 represent the means and standard deviations of five tests at each exposure time and the shaded bands represent the mean and standard deviation strength limits of the unimmersed controls. Although the immersed specimens containing indentation flaws were somewhat stronger than

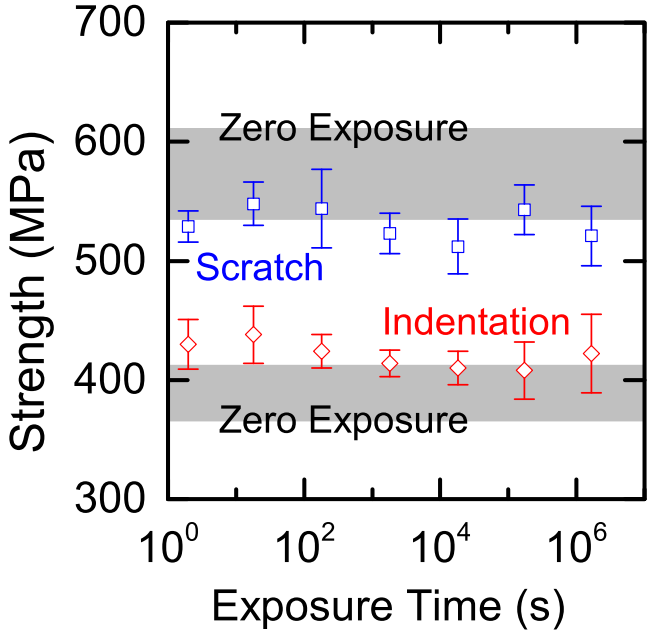


**FIGURE 10** Strength of polycrystalline $Al_2O_3$ samples containing indentation or sharp scratch flaws as a function of exposure time to water post flaw formation prior to strength testing [Color figure can be viewed at wileyonlinelibrary.com]

the controls and the immersed specimens containing scratches somewhat weaker, there was neither significant effect of exposure in either case, nor a trend in strength with increasing exposure time up to the maximum exposure of 20 days. Again, this lack of aging effect is consistent with early studies[22] and suggests that lateral crack effects were established almost immediately during indentation or scratch contact at the small loads used here.

## 4.5 | Scratch width verification

The quantitative information presented here can be used in combination to assess the severity of scratches controlling intrinsic strengths and thereby provide guidance to designers regarding the treatment and handling of $Al_2O_3$ components. In particular, the intrinsic strength distribution measurements (Figure 3), the indentation dimension measurements (Figure 4), and the scratch strength degradation measurements (Figure 6) can be combined to estimate the widths of scratches controlling intrinsic strengths. Inversion of Equation (24b) gives the effective normal contact load $<P>$ conjugate to an inert strength value, σ:

$$\langle P\rangle = [(\sigma^*/\sigma - 1)^{-1} P_*^{-1/2} - P_L^{-1/2}]^{-2}. \tag{31}$$

The effective scratch width $2w$ is then

$$2w = 2\sqrt{2}a = 2(\langle P\rangle/H)^{1/2}. \tag{32}$$

Figure 11A is a histogram of the scratch widths generated from Equations (31) and (32), the values of $\sigma^*$, $P_*$,

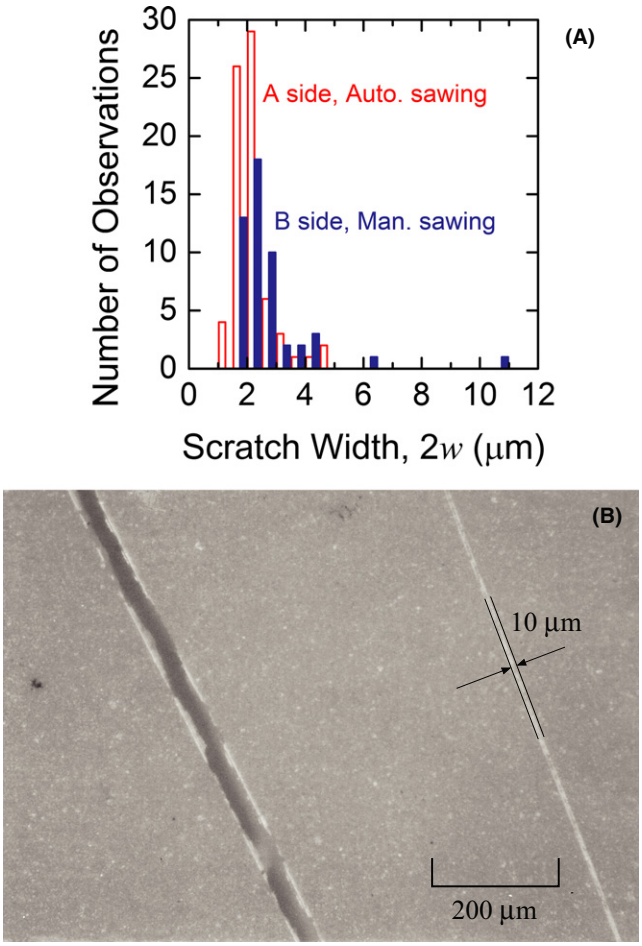


**FIGURE 11** (A) Histogram of the conjugate scratch width distribution for the intrinsic strength distributions of a polycrystalline $Al_2O_3$ shown in Figure 3. (B) Optical micrograph of the failure location of the weakest sample from the intrinsic strength distribution showing the strength-controlling scratch [Color figure can be viewed at wileyonlinelibrary.com]

$P_L$, and $H$ given above, and the intrinsic strengths given in Figure 3. The first point to note regarding Figure 11A is that the abscissa is quantitative in an absolute sense—the scratch width is specified in micrometers rather than a relative statement regarding "more severe" flaws as in section 2.2 above. This absolute specification enables direct comparison with independent measurements and in this case would provide component designers with information regarding the sizes of, or imposed loads on, particles that might give rise to scratch damage and limit intrinsic strengths. The second point to note is that the distribution of scratch widths for the B-side manually sawn samples is different from that of the A-side automatically sawn samples: The B-side samples did not exhibit very small scratches, of order 1 μm, and exhibited a few very large scratches, one of order 11 μm. Of course, these insights are consistent with the inferences drawn from the intrinsic strength distributions of Figure 3, but the quantitative nature of Figure 11A enables the scratch widths to be compared with direct observation. Figure 11B is a micrograph of the failure location of the weakest sample from the B-side distribution, presumably containing the largest scratch. It is clear that the sample failed from a large scratch preexisting on the sample surface; an adjacent scratch is indeed of width of order 10 μm, consistent with the calculations of Equations (31) and (32) and Figure 11A and providing further support for the analysis.

## 5 | DISCUSSION AND CONCLUSIONS

The analysis and experimental results presented here make clear the generality of "indentation fracture mechanics" and the indentation-strength measurement methodology. The generality was demonstrated here on the practically important case of a straight scratch flaw formed by a translated sharp contact, extending prior strength analyses[1,5,6] beyond point-localized indentation flaws. The parallel development of scratch and indentation fracture mechanics in section 3 highlights the ease of generalizing contact-induced strength degradation analyses for different flaw geometries while still including lateral crack stress-relief effects at the mesoscale and toughening effects at the microscale. For all brittle materials, incorporation of lateral crack effects in strength analyses is critical as lateral cracking and chipping is pervasive at large contacts in such materials (although the effect was not dominant here). For many polycrystalline ceramics, especially $Al_2O_3$ as studied here, incorporation of microstructurally based toughening effects into strength analyses is critical, as the small-flaw strengths in such materials are dominated by such effects, as observed in the scratch strengths of Figure 6. The deviations of the observed scratch strengths from the ideal contact flaw response in Figure 6 make clear the necessity for an expanded fracture mechanics analysis for scratch strength. Figure 6 also makes clear the advantage of using contact load as the key variable in framing an indentation-strength analysis. The load is easily controlled, thereby providing access to a range of flaw sizes and crack lengths such that different fracture phenomena can be studied [eg, the three ranges of behavior specified by Equations (26-28)]. In addition, the load is easily measured, obviating the need for crack length measurements (eg, as in Refs. [40, 42]) and ambiguity regarding residual stress state and toughening influences.

A critical feature of the analysis that enabled the variation of scratch strength to be described, Figure 6, was the scaling of the normal contact load, $P$, acting during formation of the scratch, with the load/unit length, $P_w$, characterizing the residual stress field after the scratch was formed

and during subsequent applied stressing, Equations (7) and (10). This nonlinear scaling, $P_w \sim P^{1/2}$, was a critical element omitted by Kirchner et al. in their early analyses of scratch and grinding damage and strength degradation[39,42] and although developed by Symonds et al. was not used in their study on nonequilibrium scratch failure.[19] Here, such scaling takes a central role. Similar track width equivalence analyses lead to different scaling relationships when the symmetry of the included probe angle invariance is broken. In particular, for a rolled or translated conical probe (a glass-cutting roller) in which the included probe angle varies with contact depth in the plane parallel to the translation direction, $K_{cone}=\chi_{cone}P^{2/3}/c^{1/2}$,[20] and for a rolled or translated spherical probe, in which the included probe angle varies in planes parallel and perpendicular to the translation direction, $K_{sphere}=\chi_{sphere}P^{3/4}/c^{1/2}$, [D.B. Marshall, private communication (1983)] in direct correspondence to Equation (10). Using either of these expressions for the residual SIF in section 3 further highlights the generality of the fracture mechanics analysis and leads to simple ideal strength degradation expressions for a conical roller linear contact, $\sigma_{cone} \sim P^{-2/3}$ (as observed,[18,20]) and a translated spherical contact, $\sigma_{sphere} \sim P^{-3/4}$ (to be the topic of a future work). (Such a strength relation only pertains if the translated spherical contact generates a plastic deformation track;[50] if the dragged spherical contact is elastic, cone cracks can develop along the scratch track and the strength varies as $P^{-1/3}$ in a variant of Equation (16a).[51])

Finally, from a practical point of view, scratches longer than about 30 μm and oriented at greater than about 30° to the tensile direction were able to degrade the strength of the polycrystalline $Al_2O_3$ studied here, although the maximum sustainable stress of a scratch was extremely sensitive to its length and orientation (Figures 7 and 8). Contact flaw exposure to water (Figure 10) or proximity to a free edge had no effect on the sustainable stress. All of these phenomenological observations can provide guidance to component designers using polycrystalline $Al_2O_3$ in structural applications and exposed to sharp scratches.

## ACKNOWLEDGMENTS

The author thanks Eric Liniger and Kurt Johnson for experimental assistance and Lawrence Friedman for discussion of the manuscript. Certain commercial equipment, instruments, or materials are identified in this paper in order to specify the experimental procedure adequately. Such identification is not intended to imply recommendation or endorsement by the National Institute of Standards and Technology, nor is it intended to imply that the materials or equipment identified are necessarily the best available for the purpose.

## REFERENCES

1. Cook RF. Multi-scale effects in the strength of ceramics. *J Am Ceram Soc*. 2015;98:2933-2947.
2. Lawn BR, Evans AG, Marshall DB. Elastic/plastic indentation damage in ceramics: the median/radial crack system. *J Am Ceram Soc*. 1980;63:574-581.
3. Marshall DB, Lawn BR, Evans AG. Elastic/plastic indentation damage in ceramics: the lateral crack system. *J Am Ceram Soc*. 1982;65:561-566.
4. Cook RF, Pharr GM. Direct observation and analysis of indentation cracking in glasses and ceramics. *J Am Ceram Soc*. 1990;73:787-817.
5. Marshall DB, Lawn BR. Residual stress effects in sharp contact cracking, Part 1 indentation fracture mechanics. *J Mater Sci*. 1979;14:2001-2012.
6. Marshall DB, Lawn BR, Chantikul P. Residual stress effects in sharp contact cracking, Part 2 strength degradation. *J Mater Sci*. 1979;14:2225-2235.
7. Cook RF, Roach DH. The effect of lateral crack growth on the strength of contact flaws in brittle materials. *J Mater Res*. 1986;1:589-600.
8. Knehans R, Steinbrech R. Memory effect of crack resistance during slow crack growth in notched $Al_2O_3$ bend specimens. *J Mater Sci Lett*. 1982;1:327-329.
9. Cook RF. Segregation effects in the fracture of brittle materials: Ca-$Al_2O_3$. *Acta Metall Mater*. 1990;38:1083-1100.
10. Bennison SJ, Lawn BR. Flaw tolerance in ceramics with rising crack resistance characteristics. *J Mater Sci*. 1989;24:3169-3175.
11. Cook RF, Lawn BR, Fairbanks CJ. Microstructure-strength properties in ceramics: I, effect of crack size on toughness. *J Am Ceram Soc*. 1985;68:604-615.
12. Swain MV, Lawn BR. Indentation fracture in brittle rocks and glasses. *Int J Rock Mech Min Sci Geomech Abstr*. 1976;13:311-319.
13. Almond EA, Roebuck B. Precracking of fracture-toughness specimens of hardmetals by wedge indentation. *Metals Technol*. 1978;5:92-99.
14. Almond EA, Roebuck B. The precracking of fracture toughness specimens of ceramics by wedge-indentation technique. *J Mater Sci*. 1978;13:2063-2066.
15. Swain MV, Metras JC, Guillemet CG. A deformation and fracture mechanics approach to the scoring and breaking of glass. *J Non-Cryst Sol*. 1980;3839:445-450.
16. Swain MV. The deformation associated with the scoring of soda-lime float glass with a disc cutter. *Glass Tech*. 1980;21:290-296.
17. Swain MV. Median crack initiation and propagation beneath a disc glass cutter. *Glass Tech*. 1981;22:222-230.
18. Swain MV, Metras JC. The breaking of scored glass. *Glass Tech*. 1982;23:120-124.
19. Symonds BL, Cook RF, Lawn BR. Dynamic fatigue of brittle materials containing indentation line flaws. *J Mater Sci*. 1983;18:1306-1314.
20. Cook RF. Deformation and fracture by sharp rolling contacts. *J Am Ceram Soc*. 1994;77:1263-1273.
21. Peter K. Brittle fracture and microplasticity of glass in indentation experiments (in Ger.). *Glastech Ber*. 1964;37:333-345.
22. Kirchner HP, Gruver RM, Walker RE. Strength effects resulting from simple surface treatments. In: *The Science of Ceramic*

*Machining and Surface Finishing*. Schneider Jr SJ, Rice RW, eds. Washington DC: U.S. Government Printing Office; 1972: 353-363.
23. Gruver RM, Kirchner HP. Effect of surface damage on the strength of $Al_2O_3$ ceramics with compressive Surface stresses. *J Am Ceram Soc*. 1973;56:21-24.
24. Veldkamp JDB, Hattu N, Snijders VAC. Crack formation during scratching of brittle materials. In: Bradt RC, Hasselman DPH, Lange FF, eds. *Fracture Mechanics of Ceramics*, vol. 3. New York City, New York: Plenum Press; 1978:273-301.
25. Swain MV. Microfracture about scratches in brittle solids. *Proc R Soc Lond A*. 1979;366:577-597.
26. Swain MV. Microcracking Associated with the Scratching of Brittle Solids. In: Bradt RC, Hasselman DPH, Lange FF, eds. *Fracture Mechanics of Ceramics*, vol. 3. New York City, New York: Plenum Press; 1978:257-272.
27. Kirchner HP, Gruver RM, Richard DM. Fragmentation and damage penetration during abrasive machining of ceramics. In: Hockey BJ, Rice RW, eds. *The Science of Ceramic Machining and Surface Finishing II*. Washington DC: U.S. Government Printing Office; 1979:23-40.
28. Misra A, Finnie I. On the scribing and subsequent fracturing of silicon semiconductor wafers. *J Mater Sci*. 1979;14:2567-2574.
29. Xu HHK, Jahanmir S, Wang Y. Effect of grain size on scratch interactions and material removal in alumina. *J Am Ceram Soc*. 1995;78:881-891.
30. Xu HHK, Jahanmir S. Microfracture and material removal in scratching of alumina. *J Mater Sci*. 1995;30:2235-2247.
31. Wu HZ, Roberts SG, Möbus G, Inkson BJ. Subsurface damage analysis by TEM and 3D FIB crack mapping in alumina and alumina/5vol.%SiC nanocomposites. *Acta Mater*. 2003;51:149-163.
32. Wu HZ, Roberts SG, Derby B. Residual stress distributions around indentations and scratches in polycrystalline $Al_2O_3$ and $Al_2O_3$/SiC nanocomposites measured using fluorescence probes. *Acta Mater*. 2008;56:140-149.
33. Vaudin MD, Gerbig YB, Stranick SJ, Cook RF. Comparison of nanoscale measurements of strain and stress using electron backscattered diffraction and confocal Raman microscopy. *Appl Phys Lett*. 2008;93:193116.
34. Vaudin MD, Stan G, Gerbig YB, Cook RF. High resolution surface morphology measurements using EBSD cross-correlation techniques and AFM. *Ultramicroscopy*. 2011;111:1206-1213.
35. Friedman LH, Vaudin MD, Stranick SJ, et al. Assessing strain mapping by electron backscatter diffraction and confocal Raman microscopy using wedge-indented Si. *Ultramicroscopy*. 2016;163:75-86.
36. *Guidelines for Cut Edge Quality*. Pittsburgh, PA: PPG Industries Inc; 2002.
37. *Basics Glass: Scoring and Separating Recommendations*. Corning, NY: Corning Incorporated; 2004.
38. *The Principles of Glass Cutting*. Farmington, CT: The Fletcher-Terry Company, LLC; 2010.
39. Kirchner HP, Isaacson ED. Contact damage and residual stresses induced during single point grinding of various ceramics. In: Bradt RC, Evans AG, Hasselman DPH, Lange FF, eds. *Fracture mechanics of ceramics*, vol. 5. New York City, New York: Plenum Press; 1983:57-70.
40. Kirchner HP. Comparison of single-point and multipoint grinding damage in glass. *J Am Ceram Soc*. 1984;67:347-353.
41. Conway JC Jr, Kirchner HP. The mechanics of crack initiation and propagation beneath a moving sharp indentor. *J Mater Sci*. 1980;15:2879-2883.
42. Kirchner HP, Isaacson ED. Residual stresses in hot-pressed $Si_3N_4$ grooved by single-point grinding. *J Am Ceram Soc*. 1982;65:55-60.
43. Kirchner HP. Damage penetration at elongated machining grooves in hot-pressed $Si_3N_4$. *J Am Ceram Soc*. 1984;67:127-132.
44. TECH SPECS, Coors Ceramic Company Microceramics Technical Specifications No. 31-2-0893; 1993.
45. Anstis GR, Chantikul P, Lawn BR, Marshall DB. A critical evaluation of indentation techniques for measuring fracture toughness: I, direct crack measurements. *J Am Ceram Soc*. 1985;64:533-538.
46. Cheng W, Ling E, Finnie I. Median cracking of brittle solids due to scribing with sharp indenters. *J Am Ceram Soc*. 1990;73:580-586.
47. Cook RF, Liniger EG. Grain-size effects in the indentation fracture of MgO. *J Mater Sci*. 1992;27:4751-4761.
48. Cook RF, Liniger EG, Steinbrech RW, Deuerler F. Sigmoidal indentation-strength characteristics of polycrystalline alumina. *J Am Ceram Soc*. 1994;77:303-314.
49. Lawn BR, Jakus K, Gonzalez AC. Sharp vs blunt crack hypotheses in the strength of glass: a critical study using indention flaws. *J Am Ceram Soc*. 1985;68:25-34.
50. Zhang C, Feng P, Zhang J. Ultrasonic vibration-assisted scratch-induced characteristics of C-plane sapphire with a spherical indenter. *Int J Machine Tools Manuf*. 2013;64:38-48.
51. Lawn BR, Wiederhorn SM, Roberts DE. Effect of sliding friction forces on the strength of brittle materials. *J Mater Sci*. 1984;19:2561-2569.

**How to cite this article:** Cook RF. Fracture mechanics of sharp scratch strength of polycrystalline alumina. *J Am Ceram Soc*. 2017;100:1146-1160.